



Feasibility Study of High-Velocity Oxy-fuel (HVOF) Sprayed Cermet and Alloy Coatings for Geothermal Applications

Feifei Zhang¹ · Andrew Tabecki¹ · Mike Bennett¹ · Henry Begg¹ · Stefano Lionetti² · Shiladitya Paul^{3,4}

Submitted: 22 August 2022 / in revised form: 16 January 2023 / Accepted: 29 January 2023 / Published online: 24 February 2023
© The Author(s) 2023

Abstract Geothermal is one of the least utilized renewable energy sources due to high investment costs and long development cycle. A major cost for geothermal operations is drilling, where the cost is dependent on drilling depth, tripping times, environments, etc. These costs can increase significantly for greater drilling depths, harsher environments, component failures, etc. During drilling, hammers break the rock through repetitive impact and cuttings are removed via a high-velocity stream. Component lifetime can be extended by selecting appropriate coatings resulting in reduced lost time and improved drilling efficiency. High-velocity oxygen fuel (HVOF) spraying is one of the most popular technique to deposit thick, dense and highly

adherent coatings. This paper discusses the characteristics of cermet and alloy coatings using liquid-fueled HVOF spraying technique and their performance in simulated geothermal drilling environment. Properties of the deposited cermet (WC-CoCr, CrC-NiCr) and alloy (Ni self-fluxing, Fe-based amorphous) coatings in terms of surface roughness, thickness, porosity, hardness, adhesion strength, and erosion–corrosion resistance have been studied, and their performance are compared with selected benchmarking steel used in geothermal drilling. Based on the findings of this study, recommendations are made on the type of HVOF coatings that can potentially be used in geothermal applications.

Keywords alloy · cermet · erosion–corrosion · geothermal · HVOF · thermal spraying

This article is an invited paper selected from presentations at the 2022 International Thermal Spray Conference, held May 4–6, 2022 in Vienna, Austria, and has been expanded from the original presentation. The issue was organized by André McDonald, University of Alberta (Lead Editor); Yuk-Chiu Lau, General Electric Power; Fardad Azarmi, North Dakota State University; Filofteia-Laura Toma, Fraunhofer Institute for Material and Beam Technology; Heli Koivuluoto, Tampere University; Jan Cizek, Institute of Plasma Physics, Czech Academy of Sciences; Emine Bakan, Forschungszentrum Jülich GmbH; Šárka Houdková, University of West Bohemia; and Hua Li, Ningbo Institute of Materials Technology and Engineering, CAS.

✉ Feifei Zhang
ff_zhang@hotmail.com; feifei.zhang@twi.co.uk

- ¹ Surface, Corrosion and Interface Department, TWI Ltd., Great Abington, Cambridge, UK
- ² Centro Sviluppo Materiali S.P.A., Rome, Italy
- ³ Materials and Structural Integrity Technology Group, TWI Ltd., Great Abington, Cambridge, UK
- ⁴ Materials Innovation Centre, School of Engineering, University of Leicester, Leicester, UK

Introduction

There has been an increasing challenge worldwide to meet the growing global demand for affordable, reliable and sustainable energy. The European Commission has created several energy policies, aiming to increase the share of renewable energy sources (RES) to at least 27% of the total energy consumption by 2030 and 55% by 2050. The share of electric energy consumption from RES is predicted to increase significantly, reaching as much as 97% by 2050 (Ref 1). Geothermal energy has been taking a more and more important role in the renewable energy mix, offering significant advantages such as a low carbon footprint, independent of variable climatic conditions compared to some other renewables (notably wind and solar), and the capability of providing more affordable energy. Worldwide electricity production from geothermal increased from

6833 MWe (megawatts electric) in 1995 to 9966 MWe in 2008, and direct use in 2005 displaced more than thirty million barrels of oil (Ref 2).

A major factor of the cost in deep geothermal projects relates to the drilling processes, where costs increase in proportion to the drilling depth, tripping times, harsh environments (temperature, pressure and geothermal fluid composition), etc. It is estimated that the drilling costs contribute between 30 and 70% of the overall expenditure of a deep geothermal project (Ref 3). According to a Gas Research Institute (GRI) study conducted in 1990, 48% of the drilling time of a typical well is spent on drilling the well, 27% of the time is spent changing bits or putting tubular casing in place, and 25% of the time spent measuring well and formation characteristics (Ref 4). Reducing the need for tripping times through improved component life is one of the most effective approaches for cost reduction. The drilling of deep geothermal wells involves the breakage of rock into random-sized chippings, which are required to be lifted from the base of the well to the surface. This is generally achieved with a fluid (drill mud), which is alkaline, and lifts the cuttings through a combination of viscosity and velocity. The flow in the annulus of a well bore is often turbulent, which would lead to erosion–corrosion of in-hole components through mechanical wear and chemical corrosion of fluids (both formation and introduced muds). Such effects can cause low mechanical efficiency, short component lifetime, and affect the stability and safe operation of the drilling system (Ref 5). Therefore, the application of surface coatings that can combat such effects is highly desirable (Ref 6).

Thermal spraying can deposit coatings with high hardness, dense structure and good bonding strength and is being applied as one of the commonly used processes to improve anti-corrosion and anti-wear properties of mechanical hammer parts in drilling. Compared with other coating techniques, thermal spray also offer advantages such as high productivity, robustness and cost-effectiveness (Ref 7). A lot of studies previously carried out have shown that hard thermal-sprayed coatings (such as WC-CoCr, WC-Ni) can provide good protection to drilling tools (Ref 7–11), especially against wear. The corrosion rate of WC coatings was found to increase slightly under a liquid stream environment containing solid particles (Ref 11). Among various carbide materials, WC-based coatings are usually used below 500 °C, while CrC-based coatings can be operated at temperatures up to 900 °C offering superior oxidation and corrosion resistance though with a lower hardness compared with WC coatings (Ref 12). Researchers and industries have been investigating possible alternative more cost-efficient systems with comparable resistance to mechanical and corrosive attack (Ref 13). Ni-based self-fluxing alloys were found to have the capacity of

providing good resistance to corrosion (Ref 14, 15). The development of nanocrystalline/amorphous materials attracted significant interest and was investigated as an alternative option for replacing expensive cermet coating systems (Ref 13, 16). The microstructure and properties of Ni-base self-fluxing alloys are dependent on constituents such as Cr, B, Si, C etc. The hardness is often reported to depend of the quantity of Cr and B. Carbides and Borides of Cr are usually present in sprayed coatings. Otsubo et al. carried out detailed microstructural characterization of plasma sprayed and fused coatings of Ni-Cr-B-C-Si-Fe-Mo by means of SEM, EPMA, XRD, and TEM (Ref 17). They observed different morphologies such as lumpy crystals (M_6C carbide containing Cr, Mo and Ni), two different types of rod-like crystals (M_3B_2 boride of Cr, Mo and Cr-rich M_7C_3 carbide) in addition to Ni-Ni₃B eutectic phase (Ref 17). The addition of a carbide such as $B_{13}C_2$ to the spray powder is known to increase hardness and improve wear resistance of thermally sprayed (Metco 5P gun) self-fluxing coating containing Ni, Cr, B, Si, Fe and C (Ref 18). The addition of borides in the spray powder is postulated to facilitate the precipitation of more borides. The increase in the proportion of hard phases is likely to increase the wear resistance. Post-deposition heat treatment in vacuum is also seen as a tool for decreasing porosity and improve wear resistance. Shieh et al. found that amount of pores in coatings reached 0.3 vol.% after post-heat treatment in vacuum at 950 °C (Ref 18). The combination of reduction in porosity and formation of hardphases resulted in coating hardness \sim HRC63. The interplay between spray parameters and microstructure is complex which makes prediction of properties difficult. However, several researchers have attempted to predict hardness from HVOF spraying parameters for Ni-based self-fluxing alloys. A significant amount of research has been dedicated to design of experiment (DoE) approaches, including Taguchi method (Ref 19, 20) and full-factorial design method (Ref 21). The outcome of these DoE-type activities have been mixed due to the complexities associated with the processing-microstructure-properties relationship and the vast number of variables.

In addition to Ni self-fluxing alloys, researchers have looked into Fe-based amorphous coatings for their wear and corrosion performance. It has also been proposed that Fe-based alloy amorphous coating can bridge the gap between conventional metallic alloys and ceramic hard-metal performance with combinations of corrosion resistance in seawater/chloride environment and good wear resistance (Ref 15). Some of the earliest thermal spray amorphous coatings of Fe-Ni-P-B were flame sprayed (Ref 22). These had poor adhesion (10–20 MPa) on steel substrate. Other spray systems, such as HVOF and low-pressure/high-energy plasma spraying (LPPS/HPS), have

resulted in Fe-based amorphous coatings (Fe, Cr, P, C and Mo) with better performance (Ref 17, 23). It was found that fully amorphous coating could be only obtained by LPPS for this composition (10 at.% Mo) which exhibited superior corrosion resistance than 316L stainless steel coating in 1N H₂SO₄ and 1N HCl (Ref 23). More complex compositions have also been explored, such as Fe_{49.7}Cr_{17.7}Mn_{1.9}Mo_{7.4}W_{1.6}B_{15.2}C_{3.8}Si_{2.4} (SAM2X5) and Fe₄₈Mo₁₄Cr₁₅Y₂C₁₅B₆ (SAM1651) (Ref 24). In these compositions, Cr and Mo (and W) additions provided corrosion resistance, while B enabled glass formation. Yttrium was added to the latter alloy to lower the critical cooling rate. Farmer et al. reported the corrosion rates and open-circuit potential (OCP) values of HVOF-sprayed SAM2X5 and SAM1651 coatings after corrosion testing in several environments (Ref 24). The corrosion rate data and visual examination indicated that SAM1651 might be slightly more suitable for some environments, such as seawater at 90 °C, than the SAM2X5.

The above discussion indicates that a number of publications have explored the microstructure, properties, and performance of thermal spray coatings of hardfacing carbides, self-fluxing Ni alloys, and amorphous Fe-based systems. However, studies evaluating their performance against combined erosion–corrosion degradation in geothermal drilling applications are limited. Therefore, this study focuses on carrying out a feasibility study of high-velocity oxy-fuel (HVOF)-sprayed cermet and alloy coatings for geothermal applications. Two cermet coatings (WC-CoCr and CrC-NiCr) and two alloys (Ni self-fluxing and Fe-based amorphous) coatings were prepared using liquid-fueled HVOF spraying, and their erosion–corrosion performance in simulated geothermal drilling environment were studied and compared against selected benchmarking steel.

Approach

Materials

A commonly used low alloy steel in drilling components such as piston bushing, sliding case and valve house—34CrNiMo6 was selected as a benchmark for this feasibility study. The nominal composition is shown in Table 1.

All feedstock powders including WC-CoCr, CrC-NiCr, Ni self-fluxing and Fe amorphous used for preparing various coating systems are presented in Table 2, resourced from commercial suppliers. Most of them can survive service temperatures exceeding 500 °C.

HVOF Process

The Tafa JP5000 HVOF system at TWI Ltd, manufactured by Praxair Surface Technologies, was used for coating deposition in the study. The powder was fed radially into the gun through a powder feeder. Varying the barrel length of the spray system could change the time powder resides in the nozzle. This allows the degree of melting for different powder material types to be altered. In this study, both 4 inch (101.6 mm) and 6 inch (152.4 mm) nozzles were used for different powder types. Liquid kerosene and oxygen were supplied to the spraying gun using a Tafa 5120 control console. The feedstock was fed into the gun using a Tafa model 550 hopper, and cooling water was applied and controlled using a PTC model TAE301 heat exchanger unit. The spray process in this study has been optimized from earlier work (Ref 25). Key spray parameters are presented in Table 3.

Before spraying, all the substrates were grit-blasted to remove surface contaminants and to create a rough surface for improved adhesion strength. Grit-blasting was carried out using 60 mesh brown alumina grit under 60 psi using an abrasive blasting cabinet.

Erosion–Corrosion Testing Procedures

Erosion–corrosion testing was carried out at ambient temperature (~ 20 °C) using TWI's be-spoke erosion–corrosion facility by adapting the main elements of the slurry pot equipment (Fig. 1a). The geometry of test coupons was designed to be fixed into a six-slot sample holder for carrying out in situ electrochemical measurements during the testing (Fig. 1b). The back face and edge of the test coupons were masked with epoxy resin to mask them from the test solution. An O-ring was used to seal them against the counter-bored sample wells in the wall of the carousel, with the samples being supported radially on a 200-mm diameter in the polymeric holder and exposing an area of 11.36cm² to the slurry. The sample holder was rotated at

Table 1 Nominal composition of benchmarking low alloy steel

Steel type	Composition
34CrNiMo6 (EN24T)	C 0.430, Si 0.310, Mn 0.590, P 0.009, S 0.033, Cr 1.200, Mo 0.220, Ni 1.400, Pb 0.0007, Cu 0.200, Sn 0.014, Ca 0.0029, N 0.012, Nb 0.005, Ti 0.0048, V 0.010

Table 2 Selected powders with properties suggested by suppliers

TWI ID	Materials	Powder	Compositions, wt. %	Nominal size, μm	Supplier	Manufacture process	Max temp, $^{\circ}\text{C}$
4278	WC-CoCr	Woka 3652 FC	86WC, 10Co, 4Cr	– 45 + 15, sub	Oerlikon metco	Agglomerated and sintered	500
4277	CrC-NiCr	1375VF	75Cr ₃ C ₂ , 25 NiCr	– 45 + 11	Praxair	Agglomerated and sintered	781
4279	Ni self-fluxing	1660-02	Cr 14.97, Fe3.83, Si4.42, B3.27, Ni balance	– 50 + 20	Hoganas	Gas atomized	820
4274	Fe amorphous	SHS 7574HV	C3, Cr25, B5, Mo20, Mn5, Si2, W10, Fe balance	– 53 + 20	LincolnElectric	Gas atomized	...

120 rpm, resulting in a linear flow speed of 1.25 ms^{-1} across the face of the samples in a 30L mixture of a simulated drilling fluid comprising clearbore, deionized (DI) water and NaCl (1.0 wt.%). Sodium carbonate was used to adjust the solution pH to 9.0 prior to adding abrasives. The rotational speed, in RPM, was monitored at regular intervals by an Extech Digital Photo Tachometer during testing. Sand particles with a solid load of 15wt.% were added into the fluid to simulate abrasives in the drilling condition. Sand particle morphologies are shown in Fig. 2, which is mainly composed of silica oxide and a small amount of alumina, with size distribution in the range of 0.85–1.7 mm. During testing the sample surface was exposed to various impact angles from abrasives due to its cylindrical shape and the impeller-like flow, with a total testing duration of 24 h.

In situ DC electrochemical measurements were conducted during the exposure with connections to the samples made via a six-way slip ring. Open-circuit potential (OCP) and linear polarization resistance (LPR) values were recorded against saturated calomel reference electrodes (SCE) via 3-mm diameter, 1000-mm long gel-filled, chloride-doped polymers salt bridges. A Tafel scan measurement was also carried out for each sample in the solid-free simulated drilling fluid to define the anodic and cathodic slopes of Tafel parameters (β_a and β_c values). These were used together with polarization resistance R_p to calculate the corrosion rate of the tested coating systems.

All the coated samples were tested in their as-prepared condition without application of sealant or epoxy on the test surface. Uncoated steel substrates used as benchmarking materials were ground to a 1200 grit finish using SiC papers and were then cleaned with alcohol to remove residual impurities before testing.

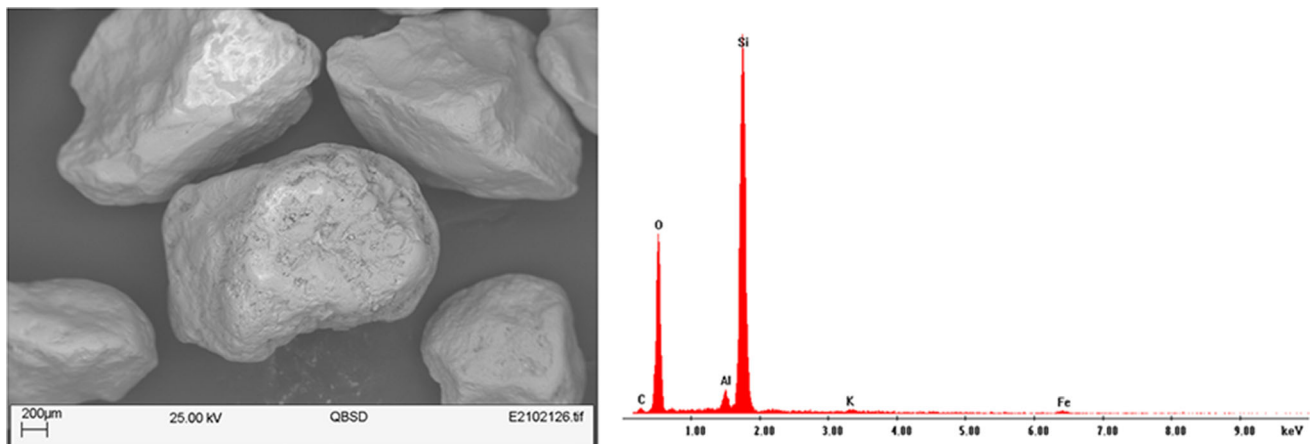
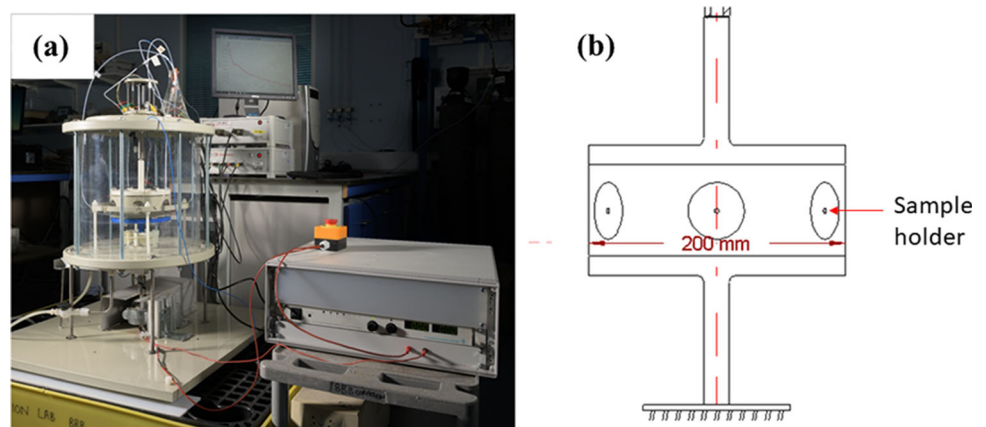
Characterization

The properties and performance of developed coatings were evaluated using a combination of the following characterization methods.

- All test coupons were recorded using a digital camera before and after testing to provide a visual comparison. Surface roughness was measured using an Alicona InfiniteFocus SL 3D surface profilometer in accordance with BS EN ISO 4288. A minimum sampling length of 2.5 mm was taken for each Ra measurement. Microstructural analysis was performed using scanning electron microscopy (SEM, Zeiss 1455EP) equipped with energy-dispersive X-ray spectroscopy (EDX, EDAX Genesis EDX system) to check performance on both top and cross-sectioned surfaces of test coupons after erosion–corrosion testing. Inspections were also

Table 3 Spray parameters for JP5000

Spray parameters	WC-CoCr coating	CrC-NiCr coating	Ni self-fluxing coating	Fe-based amorphous coating
Gun traverse speed, mm/s	900	900	900	900
Increment, mm	5	5	5	5
Nozzle, mm	152.4	152.4	101.6	101.6
Powder feed rate, g/min	95	26	35	48
Spray distance, mm	350	350	380	350
Oxygen flow, SLPM	920	873	930	873
Kerosene flow, SLPM	0.400	0.340	0.385	0.340

Fig. 1 (a) A photograph of TWI's bespoke erosion–corrosion testing facility, and (b) Design of test coupon for Geo-Drill erosion–corrosion testing**Fig. 2** SEM and EDX analyses of sand particles added into simulated drilling fluid

carried out to check whether there was any delamination occurred. The cross-sectioned samples were cold-mounted in epoxy, ground with silicon carbide papers with various grits then polished with diamond (3 and 1 μm) and colloidal silica (0.02 μm) suspensions. SEM images were taken under backscattered mode to obtain high-resolution images that show the distribution of various elements in a sample. EDX spectroscopy was

employed while imaging on SEM to obtain the elemental compositions at different areas. Optical microscopy was used to take microstructure images on the polished cross-section surfaces at the same magnifications for all samples. Coating porosity was measured according to ASTM E2109-01:2007 standard by area fraction analysis and thresholding of at least twenty (20) micrographs using ImageJ software.

Coating thickness was also measured at lower magnifications with an average value being reported.

- Hardness evaluation was done under a load of 300 g using a Duramin Vickers hardness tester in accordance with BS EN ISO 6507-1:2005 on prepared metallographic samples and was reported as an average of ten(10) measurements. The adhesion strength of deposited coatings was measured using pull-off adhesion testing according to ASTM C633. The test determines the adhesion strength of a coating to a substrate or the cohesive strength of the coating. The coated samples were bonded onto dollies with a testing area of 25.4-mm diameter using high-strength glue AV170. The testing was carried out using a tensile machine at a load of 1 mm/min. For each coating system, five(5) measurements were carried out and an average value was taken.
- Electrochemical measurements were carried out during erosion–corrosion testing to determine the contributing factors of erosion, corrosion and the synergistic effects of both on the performance of test coupons. Recordings of OCP and LPR measurements were taken each 30-min intervals from the beginning until the end of the testing. LPR could indicate the corrosion resistance of materials in an aqueous environment, by applying small voltage variations to the sample above and below its corrosion potential. Over this narrow range in the vicinity of the corrosion potential, the current response obtained is linear. The polarization resistance is defined as the slope of this current–potential curve (Ref 26). The corrosion rate (mm/year) of the sample was calculated using the following equations (Ref 27):

$$i_{\text{corr}} = \frac{\beta_a \beta_c}{2.3 R_p (\beta_a + \beta_c)} \quad (\text{Eq 1})$$

$$\text{Corrosion rate} = \mu_{\text{eq}} k_p \frac{i_{\text{corr}}}{\rho} \quad (\text{Eq 2})$$

where i_{corr} is corrosion current density. β_a and β_c are the anodic and cathodic slopes of Tafel plot, respectively. μ_{eq} is equivalent weight. k_p is a proportionality constant. ρ is density.

In addition, instantaneous corrosion rates in the absence of erosion effects were calculated for coated specimens and benchmarking steel using Tafel analysis as described above. The instantaneous data does not provide information on the evolution of corrosion processes, but it provides data on the corrosion rate at a given time.

Results and Discussions

Powder

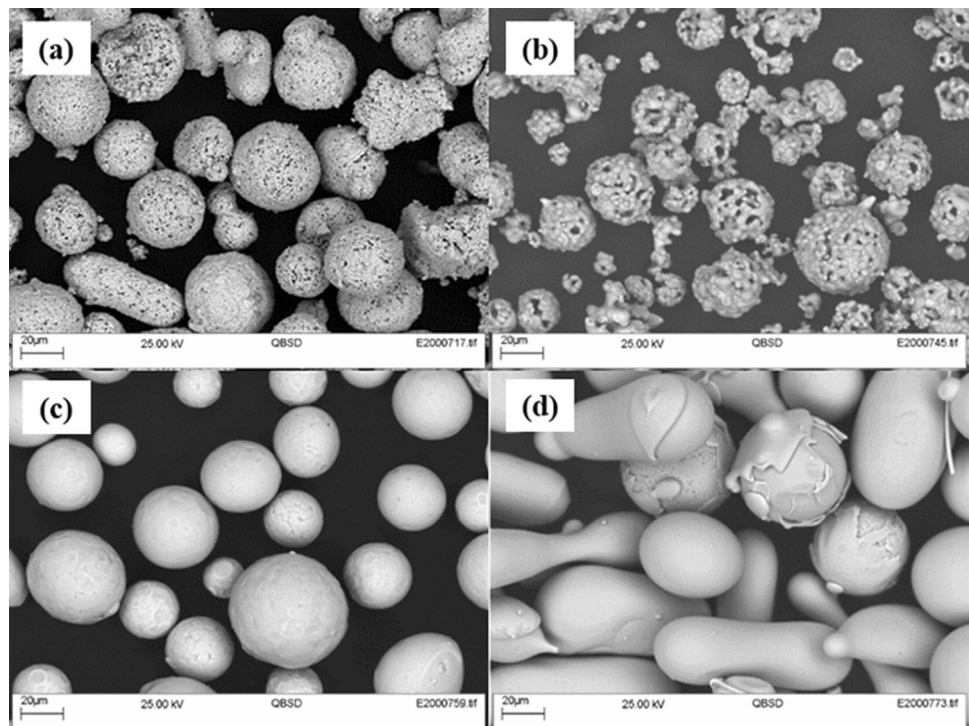
The morphology of the powders used in this study is shown in Fig. 3. Both WC-CoCr and CrC-NiCr powders were manufactured from agglomerated and sintered processes. WC-CoCr powder has a spherical and porous morphology, which is favorable for achieving good flowability during the spraying process. Only a very small proportion of irregular particles were found for WC-CoCr (Fig. 3a). CrC-NiCr powder presents a more porous agglomerated spherical morphology with many fines (Fig. 3b). When good flowability can be guaranteed, fine powders are beneficial for producing denser coatings. Ni self-fluxing powder was gas-atomized and was found to be mainly spherical (Fig. 3c). The Fe-based amorphous powder was an eight-element Fe-Cr-Mo-W-Mn-B-C-Si material that was designed to have a high glass-forming ability. Figure 3(d) indicates that this powder had mixed spherical and oval-shaped particles, which were well-alloyed, with each element homogeneously distributed in each particle.

Before Testing

Digital images of all test coupons before testing are shown in Fig. 4, with their back and edge faces being masked with epoxy resin. The surface of benchmarking steel test coupon was gently polished using 1200mesh SiC paper to remove any preexisting surface oxide layer. Surfaces for all cermet and alloy coatings were in their as-sprayed condition. These coatings presented typical surface roughness values for HVOF-sprayed coatings in a range from 3.5 ± 0.7 and $8.5 \pm 0.4 \mu\text{m}$ (Table 4). CrC-NiCr coating had the lowest surface roughness, which could be ascribed to its very fine feedstock particle size. The thickness of those deposited coatings was between 280 and 350 μm (Table 4). From porosity measurement, both WC-CoCr and CrC-NiCr coatings had low porosity, which were 0.9 ± 0.3 and $1.1 \pm 0.1\%$, respectively. The Fe-based amorphous coating had the highest porosity of $3.6 \pm 0.7\%$.

Micro-hardness measurements show that benchmarking steel in its annealed condition had a hardness of $341 \pm 12 \text{ HV}_{0.3}$ (Table 4). WC-CoCr coating had the highest hardness of $1218 \pm 112 \text{ HV}_{0.3}$ among all the coatings, while hardness for CrC-NiCr, Ni self-fluxing, and Fe-based amorphous coatings was 755 ± 72 , 661 ± 68 and $827 \pm 122 \text{ HV}_{0.3}$, respectively. From pull-off adhesion testing, adhesion strength for WC-CoCr and CrC-NiCr coatings were 64.2 ± 4.1 and $67.4 \pm 0.3 \text{ MPa}$, respectively (Table 4). Ni self-fluxing coating had the highest adhesion strength of $70.5 \pm 1.5 \text{ MPa}$, while Fe-based

Fig. 3 SEM images of as-received powders under back-scattered mode: (a) WC-CoCr, (b) CrC-NiCr, (c) Ni self-fluxing, and (d) Fe-based amorphous



amorphous coating had the lowest value at 49.4 ± 5.7 MPa.

After Testing

After 24-h erosion–corrosion testing in a simulated geothermal drilling environment, severe corrosion occurred on the surface of the benchmarking steel. About two-thirds of its surface area was covered by corrosion products (Fig. 4a). Minimal changes were observed for both WC-CoCr and Ni self-fluxing samples (Fig. 4b and d). Very little corrosion product was found on the top surface of CrC-NiCr, but this sample seemed to have experienced some minor erosion during the testing as highlighted in the circled area in Fig. 4(c). The Fe-based amorphous coated sample suffered severe corrosion during this 24-h testing (Fig. 4e). Material mass loss for these test coupons in the defined testing condition was difficult to capture and was therefore not recorded. However, thickness measurements of these coatings after 24-h testing indicated that there was very little change in thickness for various coating systems (Table 4). The reason for this little change is likely to be due to either (i) the application of the epoxy to mask the side and back of the samples, or (ii) the short duration of the tests (24 h). When epoxy was applied to mask the samples, it was suspected that this would affect the accuracy of the mass change measurement. Despite the limitations, the application of masking was to ensure that only the coated surface was tested. Another factor that would

have some bearing on the limited change in thickness is the test environment. The test conditions was not particularly harsh and was selected to simulate drilling fluids with an aim of not altering the corrosion processes significantly. Harsher test conditions are sometimes employed to accelerate corrosion, but there is always a risk that such ‘acceleration’ might lead to corrosion mechanisms not generally seen in service.

SEM and EDX analyses were performed on the surface of these test coupons, with images taken under backscattered mode to illustrate their compositional (atomic number) difference (Fig. 5). Figure 5(a) shows the morphology of porous corrosion products adhered to the surface of benchmarking steel sample. A few dark and irregularly shaped areas on the surface of WC-CoCr, CrC-NiCr and Ni self-fluxing coatings were observed (Fig. 5b, c, and d). EDX confirmed that these are abrasives from the testing solution (mainly composed of SiO_2), which had been broken into smaller pieces during the testing and were adhered to coating surfaces. However, no obvious sign of either erosion or corrosion on the surface of these coatings could be observed under SEM. The top surface of the Fe-based amorphous coating was found to be covered with a porous layer of iron oxide products (Fig. 5e).

In order to further analyze how these samples performed and whether there was any delamination or corrosion between the coating–substrate interface after this 24-h erosion–corrosion testing in a simulated geothermal environment, microstructural and chemical compositional

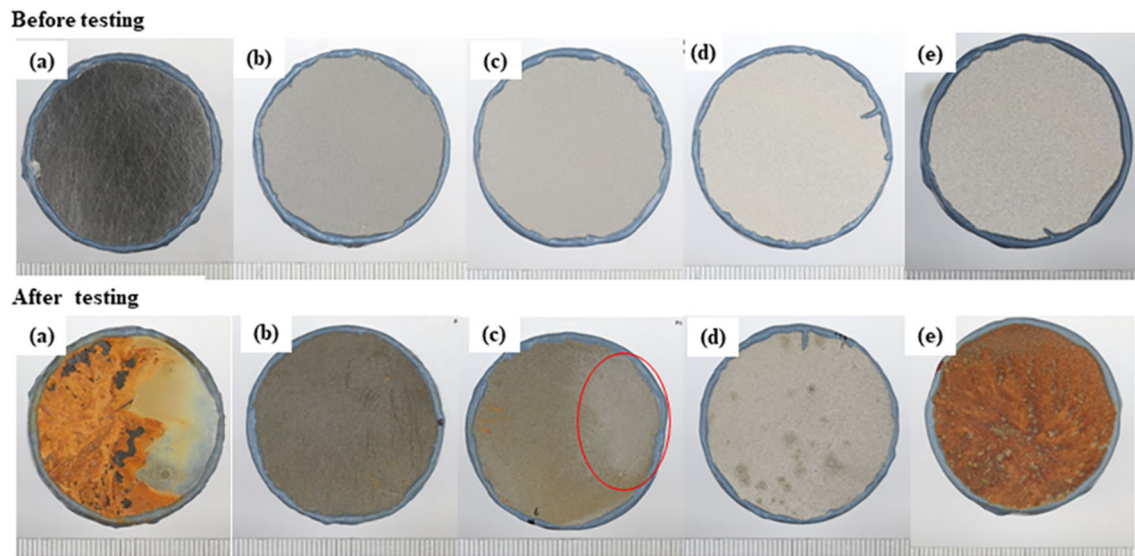


Fig. 4 Digital images of test coupons in as-prepared condition and after 24-h erosion–corrosion testing in simulated geothermal fluid: (a) benchmarking steel, (b) WC–CoCr, (c) CrC–NiCr, (d) Ni self-fluxing, and (e) Fe-based amorphous

Table 4 Characterization of steel substrate and HVOF coatings

Properties	Benchmarking steel	WC–CoCr coating	CrC–NiCr coating	Ni self-fluxing coating	Fe-based amorphous coating
Surface roughness R_a , μm	...	4.3 ± 0.5	3.5 ± 0.7	6.4 ± 0.4	8.5 ± 0.4
Thickness before testing, μm	...	341.0 ± 9.9	316.6 ± 7.9	285.6 ± 13.9	281.4 ± 12.9
Thickness after testing, μm	...	340.4 ± 3.7	315.2 ± 6.2	284.9 ± 7.3	281.6 ± 6.2
Porosity, %	...	0.9 ± 0.3	1.1 ± 0.1	2.4 ± 0.3	3.6 ± 0.7
Hardness, $\text{HV}_{0.3}$	341 ± 12	1218 ± 112	755 ± 72	661 ± 68	827 ± 122
Adhesion strength, MPa	...	64.2 ± 4.1	67.4 ± 0.3	70.5 ± 1.5	49.4 ± 5.7

analysis were also performed on their cross-sectional metallography samples. It was found that a thick corrosion layer of about $15 \mu\text{m}$ was formed on the surface of the benchmarking steel (Fig. 6a). The typical microstructure of thermal-sprayed coatings is known to be characterized by the existence of splats along with other microstructural features such as interlamellar and globular pores (due to imperfect contact and partially molten particles), intrasplat microcracks (due to stress relaxation) and splat boundaries (Ref 28). Among coated samples in this study, both WC–CoCr and CrC–NiCr coatings presented a very uniform microstructure, with a low volume fraction of fine pores scattered throughout the coating thickness (Fig. 6b and c). Some larger-sized globular pores could be observed for Ni self-fluxing coating but they were mostly non-interacting (Fig. 6d). Darker areas at the coating–substrate interface for these coatings were determined by EDX to be alumina grit from grit-blasting. No sign of corrosion product

formation was found either in the coating or at the coating–substrate interface for WC–CoCr, CrC–NiCr, and Ni self-fluxing coated samples (Fig. 6b, c, and d).

The Fe-based amorphous coating presented a high level of intersplat cracks together with some voids (globular or irregular pores) scattered across the coating thickness (Fig. 6e). A layer of corrosion product of around $20 \mu\text{m}$ was formed on the top surface of the Fe-based amorphous coating. Some corrosion product was also found at its coating–substrate interface. Its EDX pattern is in agreement with corrosion products observed previously in Fe-containing systems. The dark red–orange corrosion products observed in Fig. 4(e) could be mixtures of various oxides and hydrated oxides of Fe (Fig. 6e). The volume of the corrosion product formed should have exerted pressure at the coating–substrate interface, which resulted in the delamination of the coating from its substrate surface. This indicated that corrosion media/electrolyte had penetrated

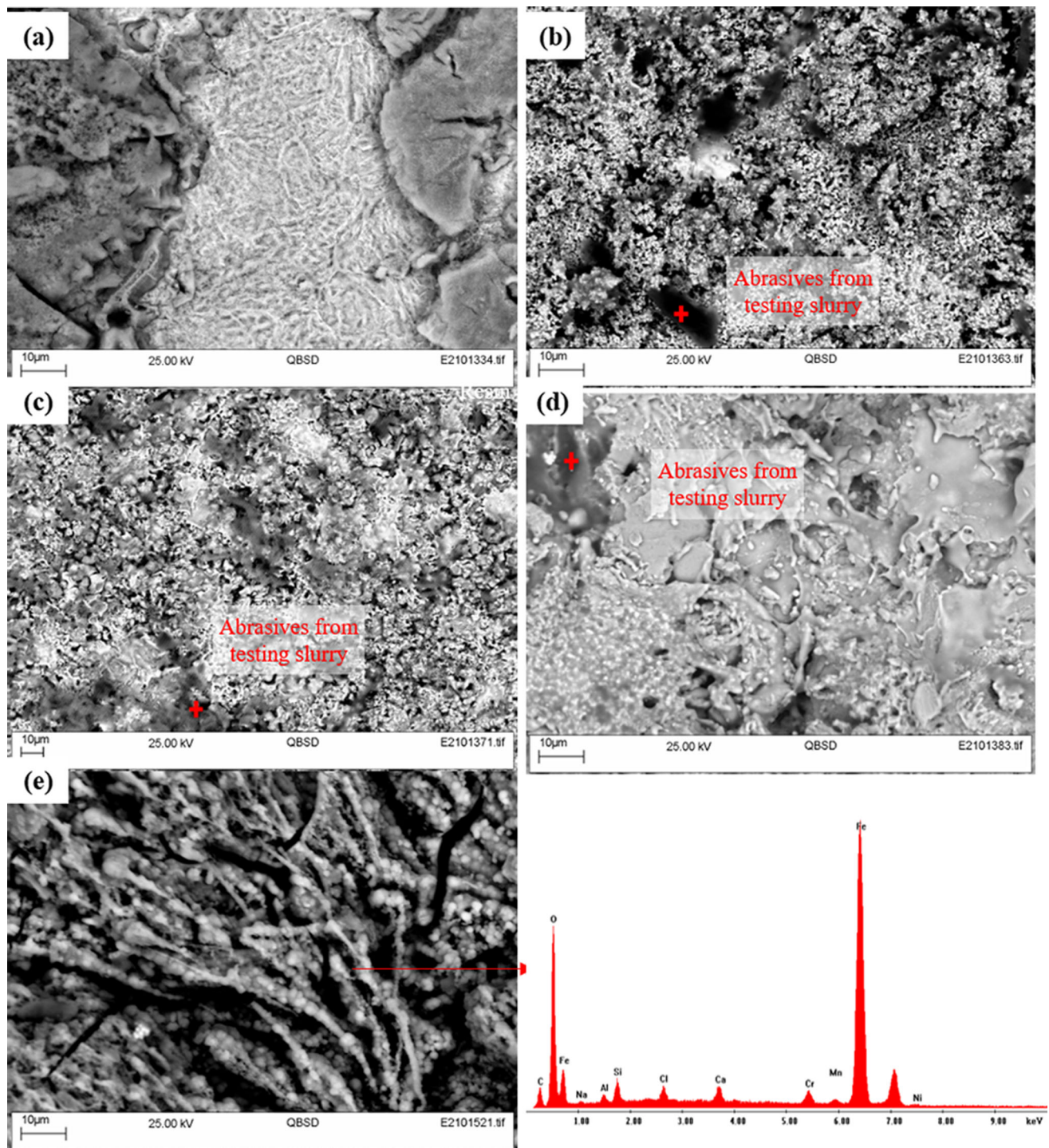


Fig. 5 SEM and EDX analyses on top surface of test coupons after 24-h erosion-corrosion testing in simulated geothermal fluid: (a) benchmarking steel, (b) WC-CoCr, (c) CrC-NiCr, (d) self-fluxing, and (e) Fe-based amorphous

onto the steel substrate through interconnected defects (cracks, voids) in the coating during this 24-h erosion-corrosion testing in the simulated geothermal fluid. Permeation of electrolyte into these pores/cracks could induce localized environments which are dramatically different from the bulk condition (i.e., pH and concentrations). This

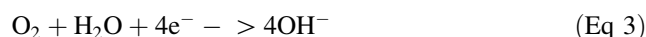
would then accelerate corrosion and corrosion-driven delamination (Ref 29). Therefore, careful design of spray parameters is critical to achieving a favorable microstructure to protect substrate materials for applications in a corrosive environment.

Electrochemical measurement results showed time dependence of open-circuit potential measurement and corrosion rate during the 24-h erosion–corrosion testing in simulated geothermal fluid (Fig. 7). Open-circuit potential showed changes for almost all the test coupons in the first 3 h of erosion–corrosion testing, which then started to gradually stabilize (Fig. 7a). Benchmarking steel presented the most negative OCP of around -600 mV when stabilized compared with HVOF cermet and alloy-coated test coupons, indicating its high activity and the tendency of corrosion in the drilling fluid. Ni self-fluxing coated sample had the most positive OCP at the initial 17 h and reached around -370 mV at 24 h. OCP curves for both CrC–NiCr and the Fe-based amorphous coatings were fairly stable, both were around -450 mV. But the Fe-based amorphous-coated sample presented a slight decrease after about 17 h with serious coating failure being observed at the end of testing as shown in Fig. 6(e). WC–CoCr coating had a sudden drop from -300 to -477 mV in the first 1.5 h. It then gradually increased to -407 mV after 12 h, and eventually increased to -317 mV and became the sample with the most positive OCP at the end of the 24-h testing duration.

From corrosion rate measurements, all HVOF-coated samples had considerably lower corrosion rates compared with benchmarking steel under erosion–corrosion conditions in the simulated geothermal drilling environment except WC–CoCr coating (Fig. 7b). Among these, Ni self-fluxing coating had the lowest corrosion rate and CrC–NiCr coating was second lowest. Though the corrosion rate for the WC–CoCr coating was of comparable level compared with benchmarking steel, it was observed from SEM and EDX analysis that WC–CoCr coating was protective to the substrate material during this 24-h erosion–corrosion testing and no sign of iron corrosion product was found from its top and cross-sectioned surfaces (Fig. 5b and 6b).

HVOF-sprayed WC coatings comprise complex microstructures which involve the formation of new and non-equilibrium phases, as well as partial carbide dissolution into the metal matrix (Ref 30). Furthermore, the behavior of WC–CoCr is dependent on the local chemistry, including pH. It is known that Co has a higher dissolution rate in acidic media, but WC is less stable in alkaline media (Ref 31). The combination of WC, Co and Cr make it difficult to predict the corrosion behavior of the composite at pH = 9 as the constituents of the coating has different corrosion behavior at different pH, and the resulting behavior would depend on the presence of each species in the vicinity of the electrolyte and their galvanic interactions. The corrosion behavior of these systems is often dependent on the presence of the binding phase at the boundary between the major constituents. If the binding phase gets actively dissolved then the WC grains might get

dislodged or removed causing a pit-like appearance (Ref 32). Another factor that might have a bearing on the corrosion performance is the presence of heterogeneities in the microstructure that can also act as active corrosion sites. In spite of the variations in the anodic reaction due to the presence of a more active metal or alloy, the most likely cathodic reaction in aerated aqueous systems is the reduction in dissolved oxygen.



This reaction increases the localized pH of the electrolyte. The consumed dissolved oxygen is however replenished in open systems by dissolution and diffusion of oxygen from air to the reaction front. HVOF-sprayed WC–CoCr have been reported to contain traces of metallic W. The presence of metallic W in a higher pH system used in the test can lead to its dissolution following the reaction:



This reaction would consume OH^- and reduce the local pH in the vicinity of any metallic W that might be present. In these local conditions, WO_2 can give rise to WO_3 which can get removed in the corrosive environment (Ref 30). However, this is difficult to be observed directly with testing slurry in the study as the sample top surface was covered with abrasives and craters were not visible from SEM images taken.

When the corrosion rate of the steel substrate and the coatings under erosion–corrosion after 24 h was compared to the values obtained from the Tafel analysis under corrosion condition (without erosion effects), more insight was obtained. The corrosion rates with and without erosion effects were found to be: 0.71 and 0.005 mm y^{-1} for bare steel; 0.615 and 0.108 mm y^{-1} for WC–CoCr coatings; 0.145 and 0.057 mm y^{-1} for CrC–NiCr coatings; 0.040 mm y^{-1} and 0.144 for Ni self-fluxing coatings; and 0.456 and 0.114 mm y^{-1} for Fe-based amorphous coatings, respectively. The above data indicate that, in general, the corrosion rate for samples tested in erosion–corrosion conditions is higher than that of samples tested in corrosion conditions alone. However, one exception was found in the case of Ni self-fluxing coatings. The reason for this disparity is unclear.

These preliminary results indicate that the failure mechanism for both HVOF-sprayed cermet and alloy samples in the erosion–corrosion testing condition (24-h testing duration, $120 \text{ rpm}/1.25 \text{ ms}^{-1}$ rotary speed, $15 \text{ wt.}\%$ sand particles in simulated clearbore-based drilling fluid) is dominated by corrosion and erosion damage to samples is negligible. Therefore, compared with coating overall integrity, coating mechanical properties such as hardness and adhesion strength seem to have less impact on sample performance. However, this may alter if testing conditions

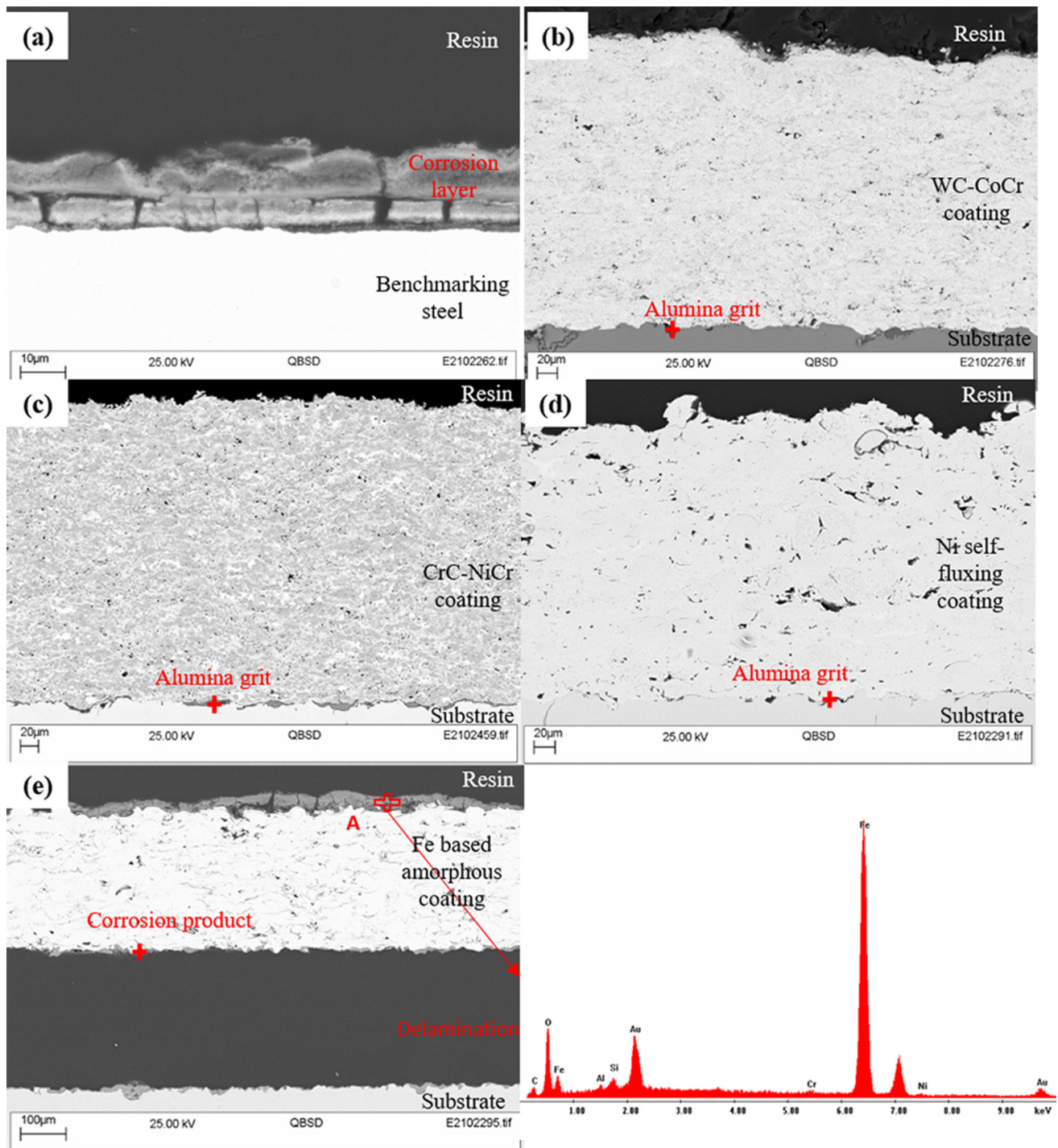


Fig. 6 SEM and EDX analyses on polished cross-sectional surface of test coupons after 24-h erosion–corrosion testing in simulated geothermal fluid: (a) benchmarking steel, (b) WC-CoCr, (c) CrC-NiCr, (d) self-fluxing, and (e) Fe-based amorphous

vary, since erosion–corrosion resistance of materials is a function of many parameters including velocity, sand loading, temperature, pH value, etc. (Ref 33). For example, when rotation speed increases, the effect of erosion of the samples might increase when compared with corrosion, thereby leading to a gradual decrease in the resistance of

the coating. Material properties, such as hardness, etc., would then play a more critical role in determining the erosion–corrosion resistance of the material (Ref 34). A more systematic study would be required to fully understand this and the behavior of pore architecture on the properties of thermal spray coatings (Ref 35).

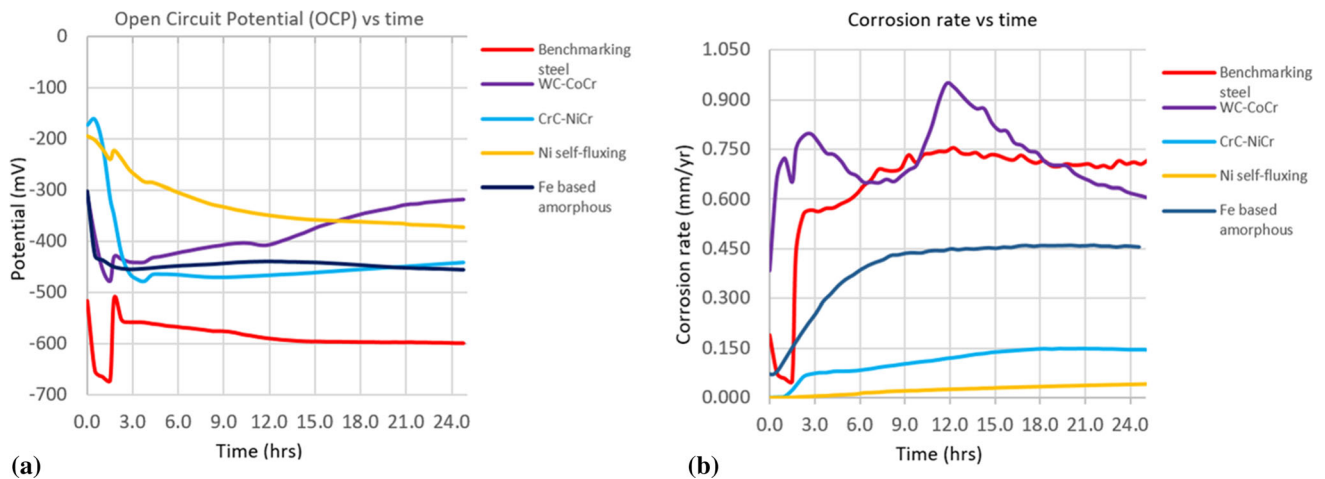


Fig. 7 Electrochemical measurements for coatings benchmarking steel after 24-h testing in simulated drilling fluid: (a) Open-circuit potential vs time, and (b) corrosion rate vs time

Conclusions

The performance of both cermet and alloy coatings was studied and compared in a simulated geothermal erosion–corrosion environment in the present work. Coatings were deposited onto a benchmarking low alloy steel using the HVOF spray technique. The conclusions of the present work are summarized below:

- The characteristics of both cermet and alloy coatings in terms of their surface roughness, coating thickness, porosity, hardness and adhesion strength were studied and discussed.
- The combined erosion–corrosion resistance of most HVOF coatings was significantly better compared with the low alloy steel. Among all, Ni self-fluxing performs the best and has the lowest corrosion rate, while Fe-based amorphous coating experienced serious delamination after 24 h of testing. WC-CoCr coating also presents effective protection to its low alloy steel substrate for the testing duration, though offering a higher corrosion rate than other coating types.
- The erosion–corrosion mechanism in the selected testing condition in geothermal fluid (24 h, 120 rpm/1.25 ms⁻¹ rotary speed, 15wt.% sand particles in clearbore-based drilling fluid) seemed to be dominated by corrosion and erosion damage to the coating was negligible.

Acknowledgments The work is part of Geo-Drill “Development of novel and cost-effective drilling technology for Geothermal Systems,” which is funded by the European Union’s Horizon 2020 research and innovation programme under grant agreement No 815319. The authors would also like to acknowledge the resources and collaborative efforts provided by the consortium of the Geo-Drill project and colleagues in the Materials Group in TWI Ltd.

Open Access This article is licensed under a Creative Commons Attribution 4.0 International License, which permits use, sharing, adaptation, distribution and reproduction in any medium or format, as long as you give appropriate credit to the original author(s) and the source, provide a link to the Creative Commons licence, and indicate if changes were made. The images or other third party material in this article are included in the article’s Creative Commons licence, unless indicated otherwise in a credit line to the material. If material is not included in the article’s Creative Commons licence and your intended use is not permitted by statutory regulation or exceeds the permitted use, you will need to obtain permission directly from the copyright holder. To view a copy of this licence, visit <http://creativecommons.org/licenses/by/4.0/>.

References

1. European commission: Energy Roadmap 2050, SEC(2011) 1565 final, Brussels, (2011) (in English). https://energy.ec.europa.eu/system/files/2014-10/roadmap2050_ia_20120430_en_0.pdf
2. J. Finger and D. Blankenship, *Handbook of Best Practices for Geothermal Drilling*, Sandia National Laboratories Albuquerque, New Mexico, 2010. (in English)
3. P. Dumas, M. Antics, and P. Ungemach, GeoElect D3.3 Report on geothermal drilling, (2013) (in English). <http://www.geoelec.eu/wp-content/uploads/2011/09/D-3.3-GEOELEC-report-on-drilling.pdf>
4. B.C. Gahan and S. Batareseh, *Laser Drilling-Drilling with the Power of Light*, Gas Technology Institute, Des Plaines, 2006. (in English)
5. F. Huang, J. Kang, W. Yue, X. Liu, Z. Fu, L. Zhu, D. She, G. Ma, H. Wang, J. Liang, W. Weng, and C. Wang, Effect of Heat Treatment on Erosion-Corrosion of Fe-Based Amorphous Alloy Coating Under Slurry Impingement, *J. Alloys Compd.*, 2020, **820**, p p153132. (in English)
6. T. Peat, A.M. Galloway, A.I. Toupis, and D. Harvey, Evaluation of the Synergistic Erosion-Corrosion Behaviour of HVOF Thermal Spray Coatings, *Surf. Coat. Technol.*, 2016, **299**, p 37–48. (in English)
7. A. Günen, Micro-Abrasion Wear Behavior of Thermal-Spray-Coated Steel Tooth Drill Bits, *Acta Phys. Pol., A*, 2016, **130**, p 217–222. (in English)

8. X. Cui, C. Wang, J. Kang, W. Yue, Z. Fu, and L. Zhu, Influence of the Corrosion of Saturated Saltwater Drilling Fluid on the Tribological Behavior of HVOF WC-10Co4Cr Coatings, *Eng. Fail. Anal.*, 2017, **71**, p 195-203. (in English)
9. B. Cheniti, D. Miroud, P. Hvizdoš, J. Balko, R. Sedláč, T. Csánádi, B. Belkessa, and M. Fides, Investigation of WC Decarburization Effect on the Microstructure and Wear Behavior of WC-Ni Hardfacing Under Dry and Alkaline Wet Conditions, *Mater. Chem. Phys.*, 2018, **208**, p 237-247. (in English)
10. Y. Zhou, X. Liu, J. Kang, W. Yue, W. Qin, G. Ma, Z. Fu, L. Zhu, D. She, H. Wang, J. Liang, W. Weng, and C. Wang, Corrosion Behavior of HVOF Sprayed WC-10Co4Cr Coatings in the Simulated Seawater Drilling Fluid Under the High Pressure, *Eng. Fail. Anal.*, 2020, **109**, p p104338. (in English)
11. J.M. Perry, A. Neville, V.A. Wilson, and T. Hodgkiess, Assessment of the Corrosion Rates and Mechanisms of a WC-Co-Cr HVOF Coating in Static and Liquid-Solid Impingement Saline Environments, *Surf. Coat. Technol.*, 2001, **137**(1), p 43-51. (in English)
12. M.M.E. Rayes, H.S. Abdo, and K.A. Khalil, Erosion-Corrosion of Cermet Coating, *Int. J. Electrochem. Sci.*, 2013, **8**, p 1117-1137. (in English)
13. H. Sarjas, A. Surzhenkov, J. Baronins, M. Viljus, R. Traksmäa, and P. Kulu, Corrosion Behavior of High Velocity Oxy-Fuel Sprayed Composite Ni/Fe-Based Self-Fluxing Alloy-Cermet Coatings, *J. Min. Metal Mater. Eng.*, 2018, **4**, p 1-9. (in English)
14. K. Bobzin, M. Öte, M.A. Knoch, X. Liao, and J. Sommer, Application of TiC reinforced Fe-based coatings by means of High Velocity Air Fuel Spraying. in *IOP Conference Series: Materials Science and Engineering, 19th Chemnitz Seminar on Materials Engineering – 19. Werkstofftechnisches Kolloquium 16-17 March 2017*, (Chemnitz, Germany, 2017), 181, p012014, (in English)
15. C. Paulin, D.L. Chicet, B. Istrate, M. Panțuru, and C. Munteanu, Corrosion behavior aspects of Ni-base self-fluxing coatings. in *IOP Conference Series: Materials Science and Engineering, 7th International Conference on Advanced Concepts in Mechanical Engineering 9-10 June 2016*, (Iasi, Romania, 2016), 147, p012034, (in English)
16. D.J. Branagan, M.C. Marshall, B.E. Meacham, I.F. Aprigliano, R. Bayles, E.J. Lemieux, T. Newbauer, F.J. Martin, J.C. Farmer, J.J. Haslam, and S.D. Day, Wear and Corrosion Resistant Amorphous/Nanostructured Steel Coatings For Replacement of Electrolytic Hard Chromium. in *Thermal Spray 2006: Proceedings of the International Thermal Spray Conference, May 15-18*, (Seattle, Washington, USA, 2006), (in English)
17. F. Otsubo, H. Era, and K. Kishitake, Structure and Phases in Nickel-Base Self-Fluxing Alloy Coating Containing High Chromium and Boron, *J. Therm. Spray Technol.*, 2000, **9**(1), p 107-113. (in English)
18. Y.H. Shieh, J.T. Wang, H.C. Shih, and S.T. Wu, Alloying and Post-Heat-Treatment of Thermal-Sprayed Coatings of Self-Fluxing Alloys, *Surf. Coat. Technol.*, 1993, **58**(1), p 73-77. (in English)
19. S.W. Rukhande and W.S. Rathod, Tribological Behaviour of Plasma and HVOF-Sprayed NiCrSiBFe Coatings, *Surf. Eng.*, 2020, **36**(7), p 745-755. (in English)
20. H. Singh, K. Goyal, and D.K. Goyal, Experimental Investigations on Slurry Erosion Behaviour of HVOF and HVOLF Sprayed Coatings on Hydraulic Turbine Steel, *Trans. Indian Inst. Met.*, 2017, **70**, p 1585-1592. (in English)
21. L. Gil and M.H. Staia, Influence of HVOF Parameters on the Corrosion Resistance of NiWCrBSi Coatings, *Thin Solid Films*, 2002, **420-421**, p 446-454. (in English)
22. H. Miura, S. Isa, and K. Omuro, Production of Amorphous Iron-Nickel Based Alloys by Flame-Spray Quenching and Coatings on Metal Substrates, *Trans. Jpn. Inst. Metals*, 1984, **25**(4), p 284-291. (in English)
23. K. Kishitake, H. Era, and F. Otsubo, Thermal-Sprayed Fe-10CM3P-7C Amorphous Coatings Possessing Excellent Corrosion Resistance, *J. Therm. Spray Technol.*, 1996, **5**, p 476-482. (in English)
24. C. Farmer, J.-S. Choi, C.K. Saw, J.J. Haslam, S.D. Day, P.D. Hailey, T. Lian, R.B. Rebak, J.H. Perepezko, J.H. Payer, D.J. Branagan, B. Beardsley, A. D'amato, and L.F. Aprigliano, Iron-Based Amorphous Metals: High-Performance Corrosion-Resistant Material Development, *Metall. Mater. Trans. A*, 2009, **40**, p 1289-1305. (in English)
25. F. Zhang and A. Tabecki, Geo-Drill D2.4 Report on drill bit tooth, fluidic oscillator, and stabilizer coating manufacture and properties, 2021, (in English). <https://cordis.europa.eu/project/id/815319/results>
26. F. Ropital, 15—Environmental degradation in hydrocarbon fuel processing plant: issues and mitigation, *Advances in Clean Hydrocarbon Fuel Processing*. M. Rashid Khan Ed., Woodhead Publishing, Amsterdam, 2011. (in English)
27. S. Paul and B. Syrek-Gerstenkorn, Can Thermally Sprayed Aluminum (TSA) Mitigate Corrosion of Carbon Steel in Carbon Capture and Storage (CCS) Environments?, *J. Therm. Spray Technol.*, 2019, **26**, p 184-194. (in English)
28. Z. Wang, A. Kulkarni, S. Deshpande, T. Nakamura, and H. Herman, Effects of Pores and Interfaces on Effective Properties of Plasma Sprayed Zirconia Coatings, *Acta Mater.*, 2003, **51**(18), p 5319-5334. (in English)
29. M.M. El Rayes, H.S. Abdo, and K.A. Khali, Erosion-Corrosion of Cermet Coating, *Int. J. Electrochem. Sci.*, 2013, **8**, p 1117-1137. (in English)
30. R. Ahmed, G. Vourlias, A. Algoburi, C. Vogiatzis, D. Chaliampalias, S. Skolianos, L.M. Berger, S. Paul, N.H. Faisal, F.L. Toma, N.M. Al-Anazi, and M.F.A. Goosen, Comparative Study of Corrosion Performance of HVOF-Sprayed Coatings Produced Using Conventional and Suspension WC-Co Feedstock, *J. Therm. Spray Tech.*, 2018, **27**, p 1579-1593. (in English)
31. S. Hochstrasser, Y. Mueller, C. Latkoczy, S. Virtanen, and P. Schmutz, Analytical Characterization of the Corrosion Mechanisms of WC-Co by Electrochemical Methods and Inductively Coupled Plasma Mass Spectroscopy, *Corr. Sci.*, 2007, **49**(4), p 2002-2020. (in English)
32. L. Zhang, Y. Chen, Q.L. Wan, T. Liu, J.F. Zhu, and W. Tian, Electrochemical Corrosion Behaviors of Straight WC-Co Alloys: Exclusive Variation in Grain Sizes and Aggressive Media, *Int. J. Refract. Metals Hard Mater.*, 2016, **57**, p 70-77. (in English)
33. W. Wan, J. Xiong, Z. Guo, L. Tang, and H. Du, Research on the Contributions of Corrosion, Erosion and Synergy to the Erosion-Corrosion Degradation of Ti(C, N)-Based Cermets, *Wear*, 2015, **326-327**, p 36-43. (in English)
34. P. Selvam Kevin, A. Tiwari, S. Seman, S.A. Beer Mohamed, and R. Jayaganthan, Erosion-Corrosion Protection Due to Cr3C2-NiCr Cermet Coating on Stainless Steel, *Coatings*, 2020, **10**(11), p 1042. (in English)
35. S. Paul, Assessing Coating Reliability Through Pore Architecture Evaluation, *J. Therm. Spray Technol.*, 2010, **19**, p 779-786. (in English)

Publisher's Note Springer Nature remains neutral with regard to jurisdictional claims in published maps and institutional affiliations.